Materials & Design 83 (2015) 344–351

Contents lists available at ScienceDirect

Materials & Design

journal homepage: www.elsevier.com/locate/matdes

Effect of sintering parameters on microstructure, mechanical properties and electrochemical behavior of Nb–Zr alloy for biomedical applications

M.A. Hussein [a,b], C. Suryanarayana [c], M.K. Arumugam [d], N. Al-Aqeeli [a,*]

[a] Department of Mechanical Engineering, King Fahd University of Petroleum & Minerals (KFUPM), Dhahran 31261, Saudi Arabia
[b] Department of Mechanical Engineering, Kafrelsheikh University, Kafrelsheikh 33516, Egypt
[c] Department of Mechanical and Aerospace Engineering, University of Central Florida, Orlando, FL 32816-2450, USA
[d] Center of Research Excellence in Corrosion, Research Institute, King Fahd University of Petroleum & Minerals (KFUPM), Dhahran 31261, Saudi Arabia

ARTICLE INFO

Article history:
Received 24 December 2014
Revised 11 April 2015
Accepted 1 June 2015

Keywords:
Spark plasma sintering
Mechanical alloying
Electrochemical testing
Nb–Zr alloy

ABSTRACT

Despite the importance of Nb–Zr alloys as candidate materials for biomedical applications, little attention has been given to their processing and the development of new or improved structures. Here, we explore the viability of synthesizing a nano/sub-micron grain structured Nb–Zr alloy through the use of mechanical alloying (MA) and spark-plasma sintering (SPS). The sintered samples were characterized through measurements of densification, Vickers hardness (HV), X-ray diffractometry (XRD) and transmission electron microscopy (TEM). The effect of the SPS parameters on the microstructure and mechanical properties of the sintered alloys was also investigated. Moreover, electrochemical corrosion analyses were performed by a means of a conventional three-electrode cell to assess the corrosion resistance of the developed alloys in Simulated Body Fluids (SBF) medium. A nano/sub-micron grain structured Nb–Zr alloy with an average grain size of between 100 and 300 nm was produced using the MA-SPS techniques. A maximum hardness and relative density of 584 *HV* and 97.9% were achieved, respectively. Moreover, the nano/sub-micron grain structured Nb–Zr alloy exhibited higher corrosion resistance in SBF medium, which makes this alloy is a promising candidate for use in biomedical applications.

1. Introduction

Nb and Zr are desirable elements for the use in biological systems and biomedical applications thanks to their biocompatibility, resistance to corrosion, mechanical integrity and ionic cytotoxicity [1,2]. Nb–Zr alloys can be processed via multiple routes, but the longstanding challenge is to develop improved microstructures that possess attractive properties. These alloys show a positive heat of mixing that has a magnitude that ranges from 6 to 17 kJ mol^{-1} [3–6]. Thus, conventional processing might not be suitable for these alloys and the use of non-equilibrium processing techniques for the development of the underlying microstructures gained considerable attention in recent years [7]. Mechanical alloying (MA) is one of the non-equilibrium processing techniques that is capable of producing alloys with improved properties, despite its simplicity. It consists of repeated cold welding, fracturing and re-welding of powder particles in a high-energy ball mill [8]. In this technique, phase diagram restrictions do not apply, and non-equilibrium phases are achieved. To date, only little attention was given to the use of MA to produce alloys made up of immiscible Zr and Nb.

One of the greatest challenges faced in powder metallurgy is identifying an appropriate sintering technique that can retain the developed microstructure while preventing or minimizing undesirable grain growth. Conventional sintering techniques usually lead to undesirable grain growth, reduced densification and loss of mechanical strength due to the long sintering time and high temperature required [9]. Among the sintering processes that have been developed thus far, SPS is proofing to be effective in yielding fully dense metallic materials at relatively low temperatures and in very short sintering times [10,11]. Such conditions are capable of preventing/reducing grain growth and minimizing the formation of undesired secondary phases that degrade the properties. Moreover, the use of SPS is straightforward and does not require pre-compaction of the starting powder. Recently, Wen et al. [12] studied the effect of sintering using Spark plasma and Vacuum arc melting on Ti–Nb–Ag alloy. The results showed that the alloy sintered by SPS possessed fracture strength values that are three times compared to the alloy sintered by conventional sintering.

* Corresponding author.
E-mail addresses: mahussein@kfupm.edu.sa (M.A. Hussein), Surya@ucf.edu (C. Suryanarayana), madhankumar@kfupm.edu.sa (M.K. Arumugam), naqeeli@kfupm.edu.sa (N. Al-Aqeeli).

http://dx.doi.org/10.1016/j.matdes.2015.06.003
0264-1275/

Furthermore, Bláhová et al. [13] successfully obtained a fine structure with enhanced mechanical properties, and higher hardness of 400 HV5 when using a combined approach of MA + SPS for Al–10Si–21Fe and Al–20Si–16Fe alloys. In general, SPS was reported [14] to facilitate the possibility of fabricating advanced alloys and composites as well as development of high precision technological parts. By using SPS, finer grain size and higher densification can be achieved at lower holding times and sintering temperatures compared to conventional sintering.

Multiple studies have considered the use of SPS to produce Nb-based alloys in different systems, for example Nb–Al, Nb–Al–W, Nb–Al–Mo and Nb–Al–N [15]. Although fully dense alloys were achieved in the Nb–Al system, inhomogeneous microstructures have been obtained in the Nb–Al–W and Nb–Al–Mo systems due to insufficient sintering time, which highlights the need for careful tuning of the SPS process [15]. Moreover, SPS has been used to produce Nb–Si–Cr and Nb–Si–B alloys and the resultant microstructure, oxidation behavior, mechanical and physical properties have been studied [16,17]. SPS has been also used to produce Nb–Si alloys with a densification exceeding 99.5% [18]. In other work [19], Nb/Nb_5Si_3 composites were successfully prepared using SPS, with the resulting alloys almost fully dense and with high compressive ductility in addition to high strength. High-density (approximately 97.7%) NbB_2 was obtained in yet another study [20] by SPS from elemental powders of Nb and B sintered at 1900 °C for a holding time of 15 min. In a recent study [21], zirconium micron-alloyed tungsten with a relative density of 97% was prepared using SPS. In their work, nanostructured ZrO_2 particles were also formed due to reaction between impurity O_2 and Zr.

As for the utilization of alloys into the biomedical field, most of the work was done on Ti–6Al–4V. In general, for the utilization of these alloys as biomedical implants, characterization usually goes beyond mechanical evaluation to include biocompatibility, toxic effect, and corrosion resistance. For the Ti64 alloy, it was reported that V and Al possess lower resistance to corrosion, have a probable toxicity [22], and possibly causing mutagenic cytology and allergic reactions [23]. Therefore, other elements were considered in the design and development of biomaterials, which included Ni and Cr. Nevertheless, Ni is showing low biocompatibility while Cr has concerns over its genotoxicity [1]. On the other hand, Zr and Nb meet the criteria for biomaterials in terms of biocompatibility, resistance to corrosion, mechanical considerations, and ionic cytotoxicity [1]. Both niobium and zirconium are highly passivating metals [24,25] and it was proven that the amount of released metallic ions from Nb–Zr alloy into physiological media is small ($<0.3\ mg\ L^{-1}$) [26]. In particular, the addition of Zr was found to result in a high level of blood compatibility when used as implants and leads to better corrosion resistance due to the formation of a stable oxide surface layer. However, little work was done to unravel the possible utilization of Nb–Zr alloys as biomedical implants and to adequately assess their properties. Some of the few literature include the work of Zhou et al. [2] in which they developed Zr–xNb alloys, where x = (2.5, 16 and 22) wt.% using vacuum arc-melting method. They studied the effect of Niobium content on the corrosion properties of the developed alloys. Their results showed that the corrosion resistance of the alloy increased by increasing Nb content. In another study, Rubitschek et al. [27] studied the corrosion resistance of ultrafine-grained (UFG) Nb–2Zr wt.% alloy processed using multipass equal channel angular processing (ECAP) in SBF. They showed that the UFG alloy possessed appreciable corrosion resistance. As the use for nanomaterials is increasing it is expected that nanophase materials would contribute significantly in the future generation biomedical implants. This is primarily due to the fact that they possess unique surfaces and exceptional mechanical properties similar to those of the human bones, in addition to offering better biocompatibility compared to coarse grain structure.

Therefore, the aim of this work is to use MA and SPS to synthesize a bulk nano/sub-micron grain structured Nb–Zr alloy for the first time with an optimized structure. The alloy will be characterized using variety of advanced techniques and will be tested for its electrochemical behavior by immersion in SBF medium. We envision that this new approach will pave the way for the development of high-performance Nb–Zr alloys for biomedical applications.

2. Materials and methods

2.1. Synthesis and consolidation of powders

The elemental Nb and Zr powders used in the current study (−325 mesh, 99.8% purity) were acquired from Alfa Aesar, USA. A nominal composition of $Nb_{60}Zr_{40}$ (values in at.%) was prepared and then milled for 10 h in a planetary ball mill (Fritsch Pulverisett 5) under an Ar atmosphere at a ball:powder ratio of 10:1. The rotational speed was 300 RPM. Both the milling vial and milling balls were made of WC without the addition of any process control agent to minimize the contamination of the milled powders. An SPS machine (FCT system-model HP D5, Germany) was used for the consolidation of the powders. The samples were sintered using a pressure of 50 MPa under vacuum and holding times of 10, 15 and 25 min were applied. To study the effect of sintering temperature on the resulting microstructure, three different temperatures – 1300, 1400 and 1500 °C – were applied at a constant heating rate of $100\ K\ min^{-1}$. Table 1 summarizes the processing conditions and combinations used. The sintering temperature was measured using a thermocouple inserted in the 20-mm-diameter sintering die of the SPS machine. 10–12 g of powder were used to produce a sample measuring approximately 20 mm in diameter and 5 mm in thickness. The die was filled with the powders and a graphite sheet was used to facilitate the removal of the specimen and to minimize the friction between the powders and die walls.

2.2. Materials' characterization

A JEOL SEM was used to study the morphology and microstructure of as-received, as—milled. XRD measurements were carried out using an AXSD8 Bruker machine with Cu Kα radiation (λ = 0.1542 nm) and a scanning speed of $1°\ min^{-1}$ (at a voltage of 40 kV and a current of 40 mA). Following SPS, the density of the sintered samples was measured based on the Archimedes' principle using a density determination kit supplied by METTLER Toledo. The reported density is the average of three measurements. Transmission Electron Microscopy (TEM: Tecnai G Series operated at 200 keV) was used to unravel the structure of the as-milled and consolidated alloys in selected cases. A digital hardness tester (Buehler, USA) was used to measure the Vickers hardness (HV) under 2-kg loads over an indentation time of 12 s. The reported hardness is the average of 10 measured values.

Table 1
SPS processing conditions.

Sample no.	Temperature (°C)	Holding time (min)	Heating rate (°C min^{-1})	Pressure (MPa)
1	1300	10	100	50
2	1300	15	100	50
3	1300	25	100	50
4	1400	10	100	50
5	1500	10	100	50
6	1300	10	50	50

2.3. Electrochemical testing

Electrochemical corrosion analyses were performed by means of a conventional three-electrode cell with the Gamry Instrument potentiostat/galvanostat/ZRA (Reference 3000). A saturated calomel electrode (SCE) was used as a reference electrode and a platinum foil as a counter electrode. The simulated human body fluid (SBF) solution was used as electrolyte for electrochemical characterization. The preparation of SBF and the procedure for conducting the experiments was adopted using an earlier report [28]. The exposed area of each sample was 1 cm^2. Electrochemical impedance spectroscopy (EIS) measurements were done in a frequency range from 100 kHz to 10 mHz with a sinusoidal AC voltage of 10 mV amplitude. The results of the EIS data are represented as a Nyquist plot. The potentiodynamic polarization curve was measured from 250 mV below the corrosion potential to 1500 mV with a scan rate of 0.197 mV s^{-1}. In order to test the reproducibility of the results, the experiments were performed in triplicate.

3. Results and discussion

The as-received starting materials and the milled product powders had different morphologies and sizes. Fig. 1(a) and (b) shows SEM images of the as-received Nb and Zr powders. Both the Nb and Zr particles exhibit different, irregular shapes and are slightly elongated. The average particle size was 22.6 and 31.0 μm for Nb and Zr, respectively. Typical SEM micrographs of milled $Nb_{60}Zr_{40}$ powders are shown in Fig. 1(c). Compared to the as-received morphology, after milling, the average particle size was reduced and the shape of the powder particles looks spherical and more uniform. However, due to the excessive cold welding and agglomeration of small particles, some large agglomerates were observed.

In order to ascertain structural differences caused by the milling process, the XRD patterns of the $Nb_{60}Zr_{40}$ powder mixtures were analyzed in the as-received and after 10 h of milling. Additionally, XRD patterns for the sintered samples are shown in Fig. 2. Sintering was carried out under a variety of sintering conditions, i.e. three different temperatures (1300, 1400 and 1500 °C) and three different holding times (10, 15, and 25 min). Under all the as-sintered conditions, typical diffraction peaks of Nb and the FCC phase were observed. In our previous work [29], the formation of the FCC phase was achieved after prolonged milling (for approximately 70 h) of $Nb_{60}Zr_{40}$ powder and was attributed to the mechanical energy imparted by the milling process as there was no consolidation involved. However, in the present work, the observed formation of the FCC phase is attributed to the substantial heating applied during SPS within a very short period of time. This effect can be explained by the equivalency between the mechanical energy and heating of the alloy to high temperature, as reported previously [8]. O. Guillon et al. [30] reported that SPS could be used in the sintering of non-equilibrium materials in their metastable state due to the exposure to high temperature and pressure in a short period of time. The resulting non-equilibrium phase combinations are primarily due to the high cooling rates associated with SPS [31]. For instance, non-equilibrium composites of cubic boron nitride-based composites were successfully obtained by SPS [32]. Also, MA of CoCrFeNiMnAl alloy led to a BCC phase, nevertheless, both FCC and BCC phases were formed after SPS [33].

Additionally, as shown in Fig. 3, the Nb(110) peak is shifted towards a lower angle due to the dissolution of Zr atoms in the Nb matrix and the formation of a Nb(Zr) solid solution [34]. By increasing the sintering time and temperature and decreasing the heating rate, the peak shift becomes more pronounced, indicating the further dissolution of Zr in the Nb matrix and the formation of a solid solution.

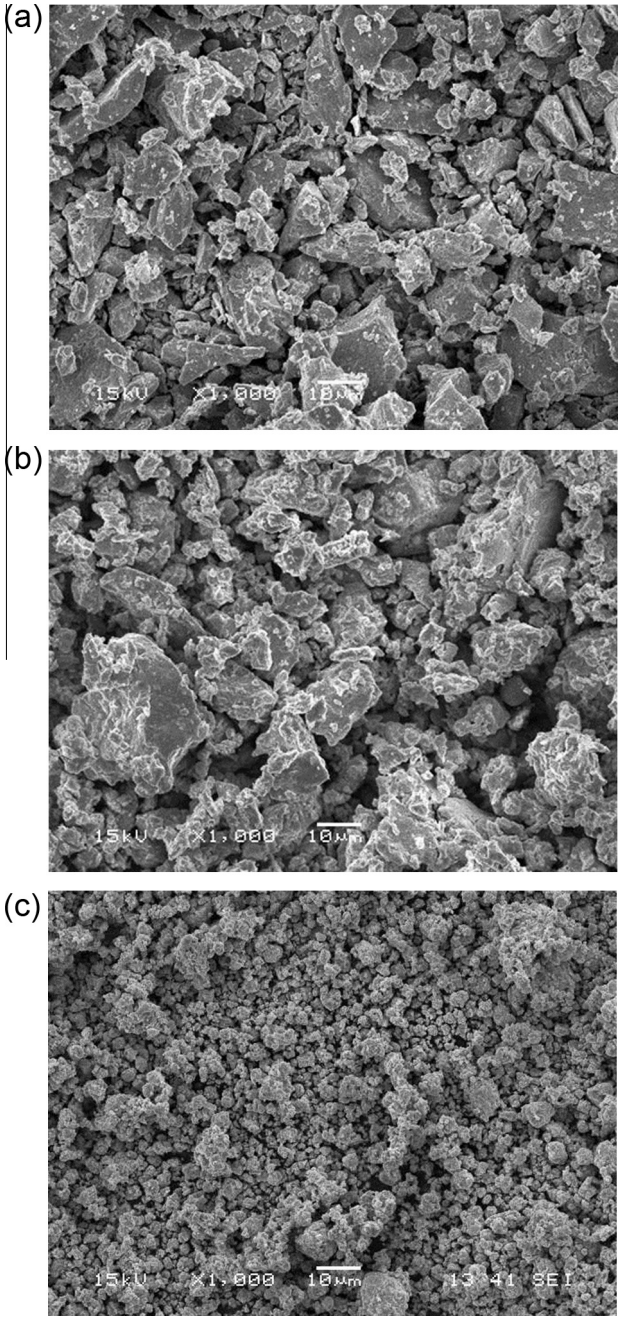

Fig. 1. SEM micrographs of as-received (a) Nb, (b) Zr powders, (c) shows $Nb_{60}Zr_{40}$ powders milled for 10 h.

The XRD patterns clearly show that the increase in SPS temperature from 1300 °C in Fig. 2, 2–1500 °C in Figs. 2–5 does not yield a major transformation in the resultant phases. The only change observed is in the relative intensity of peaks, which is triggered by the increase in temperature. The same argument also holds for the effect of increasing the holding time from 10 to 25 min, which led to a minute change in the relative intensities of peaks.

On the other hand, Fig. 4(a) shows the TEM results of the SPS sample at a temperature of 1300 °C, holding time 10 min, and heating rate of 50 °C min^{-1}. It is clear from these figures that the microstructure is not uniform and shows heterogeneous characteristics. According to the EDS analyses, the brighter regions are pure Nb, and Nb-rich solid solution (white contrast), and other regions, which contain alloyed Nb and Zr (grey contrast). The figure also

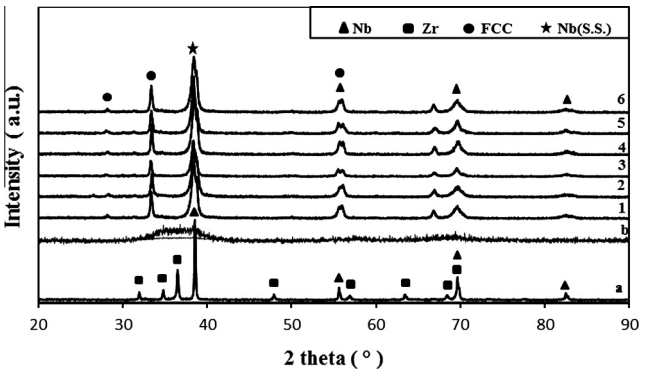

Fig. 2. XRD patterns of as-milled and SPSed Nb–Zr alloy under different conditions. (a) As-received, (b) Milled for 10 h, subjected to no SPS post-milling, (1–6) Milled for 10 h, subjected to SPS post-milling under different conditions: (1) 1300 °C, 10 min, 100 °C min^{-1}; (2) 1300 °C, 15 min, 100 °C min^{-1}; (3) 1300 °C, 25 min, 100 °C/min; (4) 1400 °C, 10 min, 100 °C/min; (5) 1500 °C, 10 min, 100 °C min^{-1}; (6) 1300 °C, 10 min, 50 °C min^{-1}.

shows the presence of equiaxed grains having an average size of 100–300 nm, which highlights the benefits of using SPS in sintering these powders and the ability to retain the developed nanostructure. In fact the presence of the nano/sub-micron grain structured alloys was reported to be promising for the use as orthopedic implants due to enhancement of osteoblast adhesion on nano-grained metals compared to coarse-grained metals [35]. Nano/sub-micron grain structured have been reported also to improve cell-material interaction, which leads to enhanced cell attachment on the nanocrystalline alloy [36], in addition to better compatibility compared to coarse-grained structure [37].

Moreover, Fig. 4(b), show the presence of stacking fault defects in the crystal structure, which is attributed to the difference in crystal structures between the alloy's constituents, i.e. Zr is HCP while Nb is BCC. The high-resolution image in Fig. 4(c) shows Moiré fringes in which the superimposed grains are showing a slight difference in orientation. SAED in Fig. 4(d) shows ring patterns recorded from relatively small-sized grains (commonly referred to as powder patterns). These spots are observed, as there are not enough grains to give a continuous ring pattern. This clearly suggests that grain sizes are not large enough to get a single crystal spot diffraction pattern.

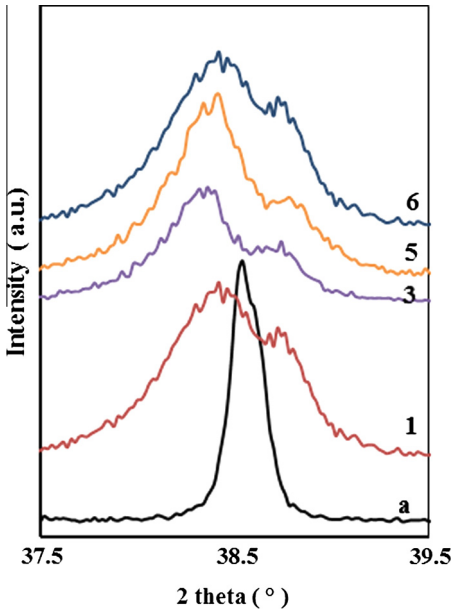

Fig. 3. The shift of the Nb(110) peak under different SPS conditions. (a) As-received, (1) 1300 °C, 10 min, 100 °C min^{-1}; (3) 1300 °C, 25 min, 100 °C min^{-1}; (5) 1500 °C, 10 min, 100 °Cmin^{-1}; (6) 1300°C, 10 min, 50 °C min^{-1}.

The consolidated samples were evaluated through microstructure, density, and Vickers hardness measurements. Fig. 5 shows the Vickers hardness and density measurements of the SPSed Nb–Zr alloy as a function of the sintering holding time; for samples sintered at 1300 °C at a heating rate of 100 °C min^{-1}. It seems that hardness decreases with the increase in holding time, with a maximum hardness value of 563.6 *HV* achieved at a 10-min holding time. This behavior is expected as the increase in holding time will lead to higher growth of the grains and ultimately lower hardness values. On the other hand, densification has increased upon increasing the holding time from 10 to 15 min, which can be related to the increased flux of heat that is associated with the increase in holding time. Nevertheless, as the holding time is increasing from 15 to 25 min the densification is slightly dropping. As the readings are given with error bars it can be concluded that the densification did not change as the holding time was increasing from 15 to 25 min. Both readings seem to be within the errors limitations and, thus, no change in densification can be concluded. It appears that increasing the holding time beyond 15 min is not needed as not much densification is achieved and the hardness seem to be decreasing as a result of having higher holding times.

To explore the effect of sintering temperature on the density and hardness of the SPS-prepared alloys, we measured the hardness and density of three samples sintered at a heating rate of 100 °C min^{-1} for a holding time of 10 min (Fig. 6). The trend exhibited by the measurements indicates that the densification is marginally increased when the sintering temperature is raised to 1500 °C; the same trend was also reported elsewhere [38,39]. However, if we consider the marginal errors in the densification measurements, it appears that temperature has no pronounced effect upon densification. In contrast, the increase in sintering temperature considerably increases hardness. This may be due to a decrease in the number of pores in the resultant sample during heating and the improved contact between the powder particles. The increase in holding time from 10 to 15 min. increases densification; which leads to an increase in grain size and results in decrease in hardness [40]. According to Hall–Petch relationship, the yield strength is dependent on the grain size and for Vickers indentation, the yield strength (σys) is related to hardness (*HV*) as $HV/\sigma ys \approx 3$. Therefore, any increase in grain size of SPSed samples can result in decrease in hardness [41]. In general, the increase in sintering temperature leads to reduction of pores and an increase in grain size, which has positive effect to increase hardness. These two effects could explain the negligible effect of temperature on the hardness as shown in Fig. 6.

To study the effect of the heating rate in densification and hardness, a sample sintered at 1300 °C for a holding time of 10 min was subjected to two different heating rates of 50 and 100 °C/min (Fig. 7). Sintering at the lower heating rate (50 °C min^{-1}) yields an alloy with a larger densification (97.9%) and hardness (568 *HV*). It appears that changing the sintering heating rate has a more pronounced effect on hardness than on density.

Fig. 8 depicts the potentiodynamic polarization curves for Nb–Zr alloys at different processing conditions in SBF medium. Results of potentiodynamic polarization exhibited quite similar polarization behaviors with the increasing potential, except some differences in the magnitude of the passive region and passive current density. These results were similar to the experimental results are in good agreement with previously published work [2] for biomedical Zr–Nb alloys. The corrosion potential (E_{corr}), the corrosion current density (i_{corr}) and calculated corrosion rate from the polarization curves are listed in Table 2. As shown in Table 2, the

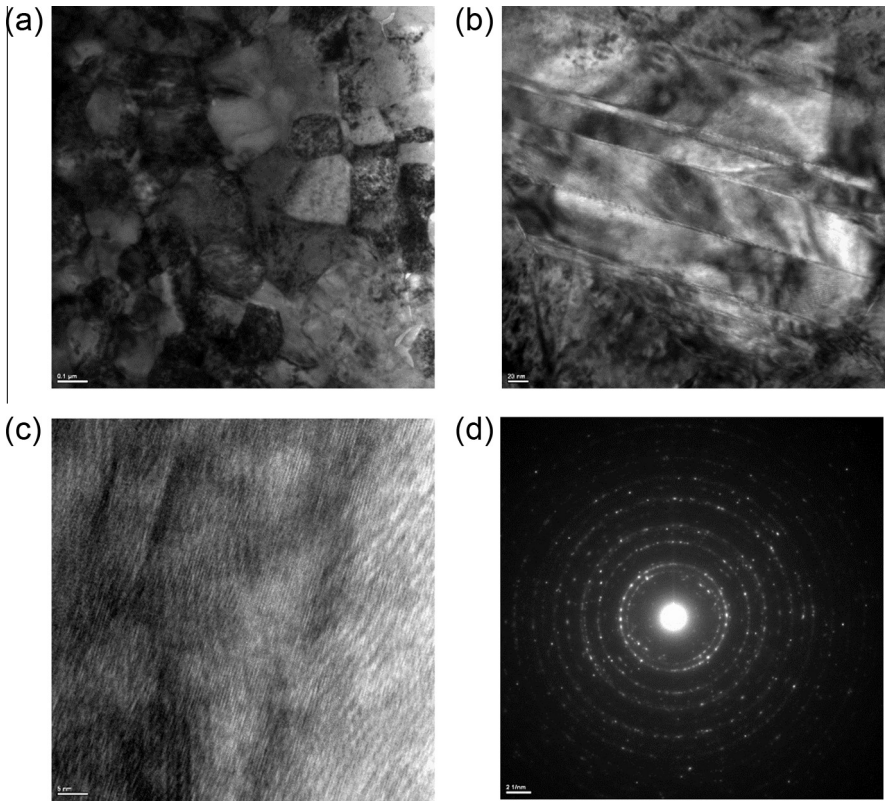

Fig. 4. The TEM results of the SPS sample at 1300 °C, holding time 10 min, and heating rate of 50 °C min^{-1}: (a) TEM image showing equiaxed grains, (b) high-resolution TEM micrograph showing stacking fault defects, (c) the presence of Moiré fringes, and (d) Selected Area Electron Diffraction (SAED) Patterns.

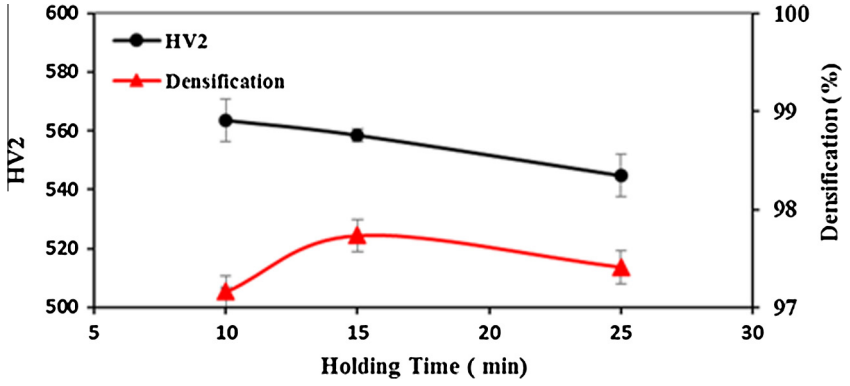

Fig. 5. Hardness and densification versus holding time of specimens sintered at 1300 °C for 100 °C min^{-1}.

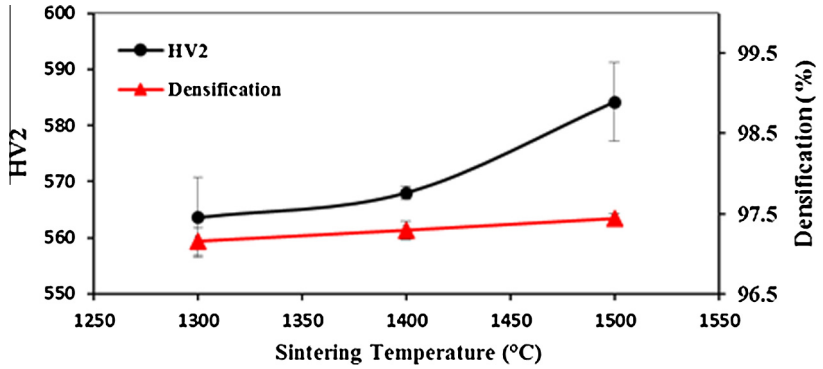

Fig. 6. Hardness and densification as a function of sintering temperature; sintering performed at 100 °C min^{-1} for 10 min.

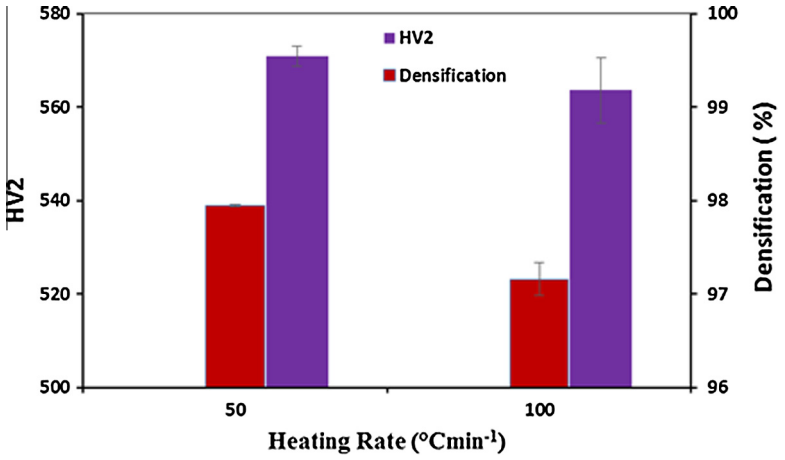

Fig. 7. Hardness and densification at different sintering heating rates for specimens sintered at 1300 °C for 10 min.

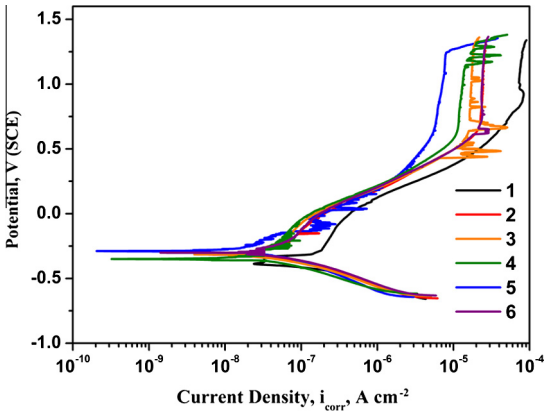

Fig. 8. Potentiodynamic polarization curves for Nb–Zr alloy at different processing conditions.

E_{corr} (vs SCE) ranking was as follows: 5 > 4 > 2 > 6 > 1 > 3. In general, a higher E_{corr} value represents a more noble metal surface and lower i_{corr} represent a better corrosion resistance [42]. Thus, Nb–Zr alloy processed at high temperature (1500 °C) has the highest corrosion resistance as compared to those of the other specimens. Besides for all the specimens investigated, the anodic branch of the polarization curve shows passive behavior associated with the protective films due to the presence of a stable region. However, the specimens at 1300 °C with the holding time of 10 min do not show obvious passive regions, which indicated the less corrosion resistance than others. Guo et al. also evaluated the effect of sintering temperature on the corrosion resistance of Ti–24Nb–4Zr–7.9Sn alloy prepared by Powder Metallurgy (PM) method and found that the samples sintered at low temperature have lower density and more porosity, and then indicate a lower corrosion resistance whereas, the samples sintered at high temperature have a higher density, a less porosity, and indicate a better corrosion resistance [26]. Accordingly, the corrosion potential is increasing with the sintering time up to 15 min and then decreases, implying that sintering time and temperature had significant alteration in corrosion behavior of investigated specimens. In particular, the specimens at sintering time of 25 min exhibited higher fluctuation in anodic branch, revealing the lower corrosion resistance in SBF medium.

Further, EIS tests were performed in order to acquire more information on the behavior of the passive films and the nature of the electrochemical processes at the interface. Fig. 9 represents Nyquist plot for Nb–Zr alloys processed at different conditions. Nyquist plots exhibit incomplete, depressed semicircles with higher diameters, which obviously suggest a near capacitive response, a passive film like an insulator [2]. In all cases, only one time constant is observed in the spectra, and thus, they could be appropriately simulated using the simplified Randles' circuit model, $R_s(Q_{dl}R_{ct})$ in the case of a single passive film formed on the metal surface. The parameters R_s and R_{ct} represented solution resistance and the charge transfer resistance, respectively.

Q_{dl} was a constant phase element (CPE), which took into account the non-ideal capacitive behavior of the film. The impedance of the CPE is given by $Z\ (\mathrm{CPE}) = [Q(jw)n]^{-1}$, where w is the angular frequency in rad/s and n is the exponential term. While Q is defined as pure capacitance for $n = 1$, resistance for $n = 0$, and inductance for $n = -1$ [43]. The fitting results of the EIS data are shown in Table 3. The fitting quality of the experimental EIS spectra to the model was recognized from the chi-squared values

Table 2
Tafel parameters for the Nb–Zr alloy specimens processed at different conditions.

Sample no.	E_{corr} (mV)	I_{corr} (μA cm^2 × 10^{-3})	β_a (mV/dec)	β_b (mV/dec)	Corr. rate (mpy) ×10^{-3}
1	−328	80.25	97	78	56.85
2	−316	34.57	83	69	28.62
3	−331	55.80	67	93	40.81
4	−312	32.40	76	94	19.42
5	−285	30.60	82	87	12.82
6	−319	41.87	92	84	33.52

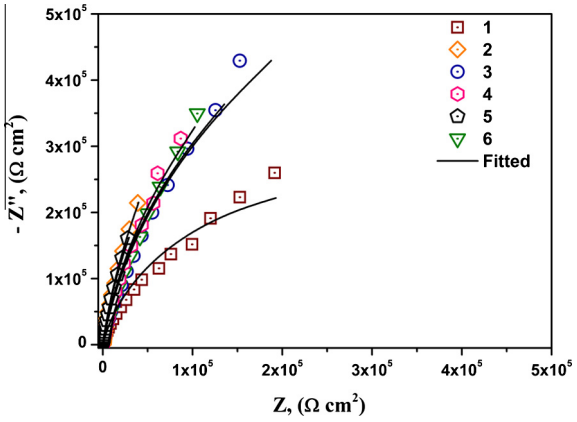

Fig. 9. Nyquist plot for the Nb–Zr alloy specimens processed at different conditions.

Table 3
EIS parameters for the Nb–Zr alloy specimens processed at different conditions.

Sample no.	R_s (Ω cm^2)	R_{ct} (kΩ cm^2)	Q_{dl} (μA cm^{-2})	n
1	86.22	564	97.14	94.24
2	80.28	2095	49.23	93.62
3	78.43	1646	68.58	92.54
4	70.50	2398	37.14	93.45
5	85.24	2685	24.35	93.48
6	74.26	1926	54.20	92.10

in the order of 10^{-6}, demonstrating the good agreement between experimental and simulated data. Calculated impedance parameters for the specimens processed at different conditions was follows as: 5 > 4 > 2 > 6 > 1 > 3, implied that the highest value of total impedance and also the lowest value of the capacitance were found to be for the specimen processed at high temperature and optimum holding time of about 15 min. In other words, the specimens prepared under these conditions showed the highest corrosion resistance among others, which may be due to the increasing of Nb–Zr density over alloy surface under these conditions.

4. Conclusions

A nano/sub-micron grain structured Nb–Zr alloy was synthesized in-situ by mechanical alloying and using a non-conventional SPS technique. The sintering pressure was fixed at 50 MPa while the sintering temperature and holding time were varied. The effects of these sintering parameters on the resulting microstructure, density, hardness, and electrochemical characteristics were studied.

1. The combination of MA and SPS proved to be a promising approach to successfully produce a nano/sub-micron grain structured Nb–Zr alloy. Specifically, the use of SPS prevented undesirable grain growth within the nano/sub-micron grain structured and resulted in a grain size between 100 and 300 nm.
2. XRD revealed the presence of Nb(Zr) solid solution and FCC. TEM, on the other hand, showed a compositionally heterogeneous structure and few stacking faults within the matrix of the alloy.
3. Hardness seems to depend on the sintering temperature and holding time, whereas density was insensitive to these variables, within error margins of the experiments. However, both hardness and density are affected by the heating rate applied during sintering; by decreasing the heating rate, both the hardness and densification increase. The developed nano/sub-micron grain structured alloy exhibits a maximum hardness of 584 HV and a relative density of 97.9%.
4. The synthesized nano/sub-micron grain structured Nb–Zr alloy exhibited higher corrosion resistance in SBF medium, implying that these alloy specimens can be used as excellent implant materials.

Acknowledgment

The authors wish to express their gratitude to the King Fahd University of Petroleum & Minerals (KFUPM) for providing financial support for this work through grant # IN111014.

References

[1] A. Biesiekierski, J. Wang, M.A. Gepreel, C. Wen, A new look at biomedical Ti-based shape memory alloys, Acta Biomater. 8 (2012) 1661–1669.
[2] F.Y. Zhou, B.L. Wang, K.J. Qiu, W.J. Lin, L. Li, Y.B. Wang, F.L. Nie, Y.F. Zheng, Microstructure, corrosion behavior and cytotoxicity of Zr–Nb alloys for biomedical application, Mater. Sci. Eng. C 32 (2012) 851–857.
[3] G. Purcek, O. Saray, F. Rubitschek, T. Niendorf, H.J. Maier, I. Karaman, Effect of internal oxidation on wear behavior of ultrafine-grained Nb–Zr, Acta Mater. 59 (2011) 7683–7694.
[4] O. Jin, Z.J. Zhang, B.X. Liu, Z.J. Zhang, B.X. Liua, Alloying behavior of formation induced by ion mixing in a system with positive heat, J. Appl. Phys. 78 (1995) 149–154.
[5] T.L. Wang, S.H. Liang, J.H. Li, K.P. Tai, B.X. Liu, Abnormal alloying behavior observed in an immiscible Zr–Nb system, J. Phys. D: Appl. Phys. 41 (2008) 095310–095316.
[6] C. Suryanarayana, J. Liu, Processing and characterization of mechanically alloyed immiscible metals, Int. J. Mater. Res. 103 (2012) 1125–1129.
[7] H.H. Liebermann, Rapidly Solidified Alloys, Marcel Dekker, New York, 1993.
[8] C. Suryanarayana, N. Al-Aqeeli, Mechanically alloyed nanocomposites, Prog. Mater. Sci. 58 (2013) 383–502.
[9] C. Camurri, M. Ortiz, C. Carrasco, Hot consolidation of Cu–Li powder alloys: a first approach to characterization, Mater. Charact. 51 (2003) 171–176.
[10] C.Y. Xu, S.S. Jia, Z.Y. Cao, Synthesis of Al–Mn–Ce alloy by the spark plasma sintering, Mater. Charact. 54 (2005) 394–398.
[11] X.L. Shi, H. Yang, S. Wang, Spark plasma sintering of W–15Cu alloy from ultrafine composite powder prepared by spray drying and calcining-continuous reduction technology, Mater. Charact. 60 (2009) 133–137.
[12] M. Wen, C. Wen, P. Hodgson, Y. Li, Fabrication of Ti–Nb–Ag alloy via powder metallurgy for biomedical applications, Mater. Des. 56 (2014) 629–634.
[13] M. Bláhová, A. Michalcová, T. František, D. Vojte, Structure and mechanical properties of Al–Si–Fe alloys prepared by short-term mechanical alloying and spark plasma sintering, Mater. Des. 75 (2015) 65–75.
[14] R. Orru, R. Licheri, A.M. Locci, A. Cincotti, G. Cao, Consolidation/synthesis of materials by electric current activated/assisted sintering, Mater. Sci. Eng. R Reports 63 (4–6) (2009) 127–287.
[15] T. Murakami, A. Kitahara, Y. Koga, M. Kawahara, H. Inui, M. Yamaguchi, Microstructure of Nb–Al powders consolidated by spark plasma sintering process, Mater. Sci. Eng. A 239–240 (1997) 672–679.
[16] T. Murakami, S. Sasaki, K. Ichikawa, A. Kitahara, Oxidation resistance of powder compacts of the Nb–Si–Cr system and $Nb_3Si_5Al_2$ matrix compacts prepared by spark plasma sintering, Intermetallics 9 (2001) 629–635.
[17] T. Murakami, C.N. Xu, A. Kitahara, M. Kawahara, Y. Takahashi, Microstructure, mechanical properties and oxidation behavior of powder compacts of the Nb–Si–B system prepared by spark plasma sintering, Intermetallics 7 (1999) 1043–1048.
[18] W. Liu, Y. Fu, J. Sha, Microstructure and mechanical properties of Nb–Si alloys fabricated by spark plasma sintering, Progr. Nat. Sci.: Mater. Int. 23 (2013) 55–63.
[19] C.L. Ma, A. Kasama, Y. Tan, H. Tanaka, R. Tanaka, Y. Mishima, S. Handa, Synthesis of Nb/Nb_5Si_3 in-situ composites by mechanical milling and reactive spark plasma sintering, Mater. Trans., JIM 41 (2000) 719–726.
[20] K. Sairam, J.K. Sonber, T.S.R.C. Murthy, C. Subramanian, R.K. Fotedar, R.C. Hubli, Reaction spark plasma sintering of niobium diboride, Int. J. Refract. Met. Hard Mater. 43 (2014) 259–262.
[21] Z.M. Xie, R. Liu, Q.F. Fang, Y. Zhou, X.P. Wang, C.S. Liu, Spark plasma sintering and mechanical properties of zirconium micro-alloyed tungsten, Nucl. Mater. 44 (2014) 175–180.
[22] Ana Lucia Roselino Ribeiro, Rubens Caram Junior, Flavia Farias Cardoso, Romeu Belon Fernandes Filho, Luís Geraldo Vaz, Mechanical, physical, and chemical characterization of Ti–35Nb–5Zr and Ti–35Nb–10Zr casting alloys, J. Mater. Sci.: Mater. Med. 20 (2009) 1629–1636.
[23] K. Niespodziana, K. Jurczk, M. Jurczk, The synthesis of titanium alloys for biomedical applications, Rev. Adv. Mater. Sci. 18 (2008) 236–240.
[24] H. Ahn, D. Lee, C.-W. Moon, K.-M. Lee, K. Lee, A study about the biocompatibility of Ti–8Ta–3Nb alloys with surface modification, Surf. Coat. Technol. 202 (2008) 5779–5783.
[25] X.J. Wang, Y.C. Li, J.Y. Xiong, P.D. Hodgson, C.E. Wen, Porous TiNbZr alloy scaffolds for biomedical applications, Acta Biomater. 5 (2009) 3616–3624.
[26] Shibo Guo, Aimin Chu, Haijiang Wu, Chunbo Cai, Xuanhui Qu, Effect of sintering processing on microstructure, mechanical properties and corrosion resistance of Ti–24Nb–4Zr–7.9Sn alloy for biomedical applications, J. Alloys Compd. 597 (2014) 211–216.
[27] F. Rubitschek, T. Niendorf, I. Karaman, H.J. Maier, Corrosion fatigue behavior of a biocompatible ultrafine-grained niobium alloy in simulated body fluid, J. Mech. Behav. Biomed. Mater. 5 (2012) 181–192.
[28] T. Kokubo, H. Takadama, How useful is SBF in predicting in-vivo bone bioactivity, Biomaterials 27 (2006) 2907–2915.
[29] N. Al-Aqeeli, C. Suryanarayana, M.A. Hussein, Formation of an amorphous phase and its crystallization in the immiscible Nb–Zr system by mechanical alloying, J. Appl. Phys. 114 (2013) 153512–153514.
[30] O. Guillon, J. Gonzalez-Julian, B. Dargatz, T. Kessel, G. Schierning, J. Räthel, M. Herrmann, Field-assisted sintering technology/spark plasma sintering: mechanisms, materials, and technology developments, Adv. Eng. Mater. 16 (7) (2014) 830–849.
[31] F. Zhang, M. Reich, O. Kessler, E. Burkel, The potential of rapid cooling spark plasma sintering for metallic materials, Mater. Today 16 (5) (2013) 192–197.
[32] J.C. Garrett, I. Sigalas, M. Herrmann, E.J. Olivier, J.H. O'Connell, CBN reinforced Y-α-SiAlON composites, J. Eur. Ceram. Soc. 33 (11) (2013) 2191–2198.

[33] C. Wang, W. Ji, Z. Fu, Mechanical alloying and spark plasma sintering of CoCrFeNiMnAl high-entropy alloy, Adv. Powder Technol. 25 (4) (2014) 1334–1338.
[34] N. Al-Aqeeli, M.A. Hussein, C. Suryanarayana, Phase evolution during high energy ball milling of immiscible Nb–Zr alloys, Adv. Powder Technol. 26 (2015) 385–391.
[35] S. Faghihi, A.P. Zhilyaev, J.A. Szpunar, F. Azari, H. Vali, M. Tabrizian, Nanostructuring of a titanium material by high-pressure torsion improves pre-osteoblast attachment, Adv. Mater. 19 (2007) 1069–1073.
[36] D. Khang, J. Lu, C. Yao, K.M. Haberstroh, T.J. Webster, The role of nanometer and sub-micron surface features on vascular and bone cell adhesion on titanium, Biomaterials 29 (2008) 970–983.
[37] T.J. Webster, J.U. Ejiofor, Increased osteoblast adhesion on nanophase metals: Ti, Ti6Al4V, and CoCrMo, Biomaterials 25 (2004) 4731–4739.
[38] G.M. Le, a. Godfrey, N. Hansen, Structure and strength of aluminum with sub-micrometer/micrometer grain size prepared by spark plasma sintering, Mater. Des. 49 (2013) 360–367.
[39] Z.-F. Liu, Z.-H. Zhang, J.-F. Lu, A.V. Korznikov, E. Korznikova, F.-C. Wang, Effect of sintering temperature on microstructures and mechanical properties of spark plasma sintered nanocrystalline aluminum, Mater. Des. 64 (2014) 625–630.
[40] A. Domı, A. Lara, A.L. Ortiz, A. Mun, Densification of additive-free polycrystalline b – SiC by spark-plasma sintering, Ceram. Int. 38 (2012) 45–53.
[41] N. Saheb, Spark plasma and microwave sintering of Al6061 and Al2124 alloys, Int. J. Miner., Metall. Mater. 2 (2013) 152–159.
[42] A. Madhan Kumar, P. Sudhagar, S. Ramakrishna, Y. Kang, H. Kim, Z. Gasem, N. Rajendran, Evaluation of chemically modified Ti–5Mo–3Fe alloy surface: electrochemical aspects and in-vitro bioactivity on MG63 cells, Appl. Surf. Sci. 307 (2014) 52–61.
[43] Yong-yuan Guo, Meng-qi Cheng, De-sheng Chen, Xiao-bing Xue, Xian-long Zhang, In vitro corrosion resistance and cytotoxicity of novel TiNbTaZr alloy, Trans. Nonferrous Met. Soc. China 22 (2012) 175–180.